



Published in final edited form as:

Neuroimage. 2017 September ; 158: 26–36. doi:10.1016/j.neuroimage.2017.06.069.

Correction of Metal-Induced Susceptibility Artifacts for Functional MRI during Deep Brain Stimulation

Myung-Ho In^{1,2}, Shinho Cho¹, Yunhong Shu², Hoon-Ki Min^{1,2,3}, Matt A. Bernstein^{2,3}, Oliver Speck^{4,5,6,7}, Kendall H. Lee^{1,3}, and Hang Joon Jo^{1,8,*}

¹Department of Neurologic Surgery, Mayo Clinic, Rochester, Minnesota, USA

²Department of Radiology, Mayo Clinic, Rochester, Minnesota, USA

³Departments of Physiology and Biomedical Engineering, Mayo Clinic, Rochester, Minnesota, USA

⁴Department of Biomedical Magnetic Resonance, Institute for Experimental Physics, Otto-von-Guericke University Magdeburg, Germany

⁵German Centre for Neurodegenerative Diseases (DZNE), Site Magdeburg, Germany

⁶Leibniz Institute for Neurobiology, Magdeburg, Germany

⁷Center for Behavioral Brain Sciences, Magdeburg, Germany

⁸Department of Neurology, Mayo Clinic, Rochester, Minnesota, USA

Abstract

Functional magnetic resonance imaging (fMRI) is an emerging tool for investigating brain activation associated with, or modulated by, deep brain stimulation (DBS). However, DBS-fMRI generally suffers from severe susceptibility to artifacts in regions near the metallic stimulation electrodes, as well as near tissue/air boundaries of the brain. These result in strong intensity and geometric distortions along the phase-encoding (PE) (i.e., blipped) direction in gradient-echo echo-planar imaging (GE-EPI). Distortion presents a major challenge to conducting reliable data analysis and in interpreting the findings. A recent study showed that the point spread function (PSF) mapping-based reverse gradient approach has a potential to correct for distortions not only in spin-echo EPI, but also in GE-EPI acquired in both the forward and reverse PE directions. In this study, we adapted that approach in order to minimize severe metal-induced susceptibility artifacts for DBS-fMRI, and to evaluate the performance of the approach in a phantom study and a large animal DBS-fMRI study. The method combines the distortion-corrected GE-EPI pair with geometrically different intensity distortions due to the opposing encoding directions. The results demonstrate that the approach can minimize susceptibility artifacts that appear around the metallic electrodes, as well as in the regions near the tissue/air boundaries in the brain. We also

*Corresponding Author Information: Hang Joon Jo, Ph.D. jo.hang@mayo.edu, 200 First Street SW, Rochester, MN 55905, USA.

Publisher's Disclaimer: This is a PDF file of an unedited manuscript that has been accepted for publication. As a service to our customers we are providing this early version of the manuscript. The manuscript will undergo copyediting, typesetting, and review of the resulting proof before it is published in its final citable form. Please note that during the production process errors may be discovered which could affect the content, and all legal disclaimers that apply to the journal pertain.

demonstrated that an accurate geometric correction is important in improving BOLD contrast in the group dataset, especially in regions where strong susceptibility artifacts appear.

Keywords

Point spread function; reverse gradient approach; susceptibility artifacts; metallic artifacts; fMRI; deep brain stimulation (DBS); geometric distortion; intensity distortion

Introduction

Functional magnetic resonance imaging (fMRI) is a promising tool for better understanding the largely unknown mechanisms related to the therapeutic effects of deep brain stimulation (DBS). Recently, several studies (Gibson et al., 2016a; Gibson et al., 2016b) have reported on the benefits of fMRI in investigating novel insights of the underlying mechanisms in patients with implanted DBS devices. However, only a limited number of DBS-fMRI studies involving patients have been reported. Alternatively, using large animals as study models for fMRI has become a useful platform for translational studies investigating the global and local neuromodulatory effects of DBS (Min et al., 2012; Kim et al., 2013; Knight et al., 2013; Ross et al., 2016).

Applications to both animal and human subjects with implanted DBS, however, has faced substantial and unique challenges, which include radiofrequency (RF)-induced heating and the production of strong susceptibility artifacts near the metallic DBS electrode leads and connectors that are implanted in the brain. Although careful attention to set up and conduction of DBS-fMRI experiments is still required due to specific absorption rate (SAR) restrictions with DBS electrodes, safety concerns associated with heating effects may be manageable even at 3T, as shown in a previous study (Gorny et al., 2013). However, the latter concern still poses a substantial challenge in terms of performing reliable data analysis and interpreting the data. Due to strong susceptibility changes between tissue and the metallic DBS electrodes used for electrical stimulation, signal dropouts and strong geometric distortions generally occur in the affected area, which results in poor image quality as well as a degradation of blood-oxygen-level-dependent (BOLD) contrast in DBS-fMRI. In addition, the effects become more severe at higher field such as 3T, despite the increased signal to noise ratio (SNR).

The reverse gradient approach (Andersson et al., 2003; Morgan et al., 2004; Meara et al., 2008; Embleton et al., 2010; Holland et al., 2010) has been proposed to minimize geometric distortions as well as loss of spatial information in compressed regions. In these approaches, a pair of EPIs with opposite phase-encoding (PE) polarity (i.e. forward (blip-up) and reverse (blip-down) k-space traversal leading to opposite geometric distortions) are acquired, used for calculating a distortion map, and combined after distortion correction with the distortion map. The loss of spatial information due to image compression can be compensated based on the corresponding image with the opposite distortions. The combination of the distortion-corrected EPI pair can resolve the local loss of spatial information. However, since strong image compression leads to severe signal dropout due to destructive interference in GE-EPI (rather than the signal summation of compressed voxels as in spin-echo EPI (SE-EPI)), the

reverse gradient approach generally works only well on SE-EPIs with opposite distortions (In et al., 2015). Geometric distortions in GE-EPIs with opposite PE polarity could be calculated based on a corresponding pair of SE-EPIs (Holland et al., 2010). Such an application, however, may not be suitable for DBS-fMRI due to very conservative SAR-limitations associated with DBS electrodes. Recently, a point-spread-function (PSF) mapping-based reverse gradient approach (In et al., 2015) was proposed to correct distortions in diffusion imaging applications. In distinction to other reverse gradient approaches (Andersson et al., 2003; Morgan et al., 2004; Meara et al., 2008; Embleton et al., 2010; Holland et al., 2010), this approach can correct distortions not only in SE-EPIs, but also in GE-EPIs with opposite PE polarities using a single 3D PSF reference dataset acquired for only one PE direction.

In this work, the PSF mapping-based reverse gradient approach was adapted for use in DBS-fMRI applications in order to minimize the metal-induced susceptibility artifacts that are produced near the metallic DBS components, especially the electrodes. Since an investigation of the theoretical basis for SE-EPI was essentially reported in a previous study (In et al., 2015), an additional investigation for GE-EPI and an evaluation of the performance was performed in a phantom and in-vivo swine brain with implanted DBS. To demonstrate the efficiency for DBS-fMRI applications, nucleus accumbens (NAc) DBS-fMRI experiments were performed in swine. The data were evaluated qualitatively and quantitatively for each individual, as well as the entire group.

Material and Methods

PSF mapping-based reverse gradient approach for GE-EPI

In the following, a brief review of the PSF mapping-based reverse gradient approach is presented, followed by a theoretical background depicting why this approach is applicable, with the extension to GE-EPI. Because an additional PSF- (or spin-warp) PE is added to the conventional 2D-EPI sequence, the PSF mapping sequence acquires 3D k -space data including a readout (x) and two PE, PSF-PE (s) and EPI-PE (y), dimensions, respectively suffering from negligible, no, and strong geometric distortions (Chung et al., 2011; In and Speck, 2012). The spin-warp PE is wrapped around the EPI in a conventional manner and this dimension (s) is distortion-free. Neglecting distortion in the readout dimension, the reconstructed 3D PSF data can be simplified as a 2D PSF image $I(s,y)$ at a given x position (Figs. 1A–a and 1B–a):

$$I(s,y)=\rho(s)M(s-y-\Delta B(s)), \quad (1)$$

where ρ is the proton density, and M is the PSF with shift $B(s)$ and degree of blurring at each voxel due to field inhomogeneity effects. Due to the shifts of PSFs $B(s)$, interestingly, both non-distorted $I(s)$ (Figs. 1A–c and 1B–c) and distorted reference images $I(y)$ (Figs. 1A–b and 1B–b) can be obtained from a 3D PSF data by integration along the y - and s -directions, respectively (Robson et al., 1997; Chung et al., 2011) :

$$I(s) = \int I(s, y) dy, \quad (2)$$

$$I(y) = \int I(s, y) ds, \quad (3)$$

Reverse phase-encoded PSF data with opposite distortions $I_r(s, y)$ can also be obtained simply by mirroring of the PSFs in Eq. 1 with $-B(s)$ along the y -direction about the diagonal line (Fig. 1C–a), which is required to calculate the distortion information to correct for the reverse GE-EPI with opposite geometric distortions (In et al., 2015):

$$I_r(s, y) = \rho(s) M(s - y + \Delta B(s)). \quad (4)$$

Measurements of the PSF profile in the compressed regions

Reliable measurements of the PSF profile from the 3D PSF data are particularly important in this approach for the accurate correction of both GE-EPIs with opposite distortions, since the measured PSF profile in the distorted coordinate (y) is used as a kernel for distortion correction (In and Speck, 2012). As opposed to SE-EPI, however, summation of the compressed voxels generally causes strong signal dropout in GE-EPI due to the intravoxel dephasing effect of the combined voxels (green arrow in Fig. 1E–d), which results in a residual intensity mismatch between the pair of distortion-corrected GE-EPIs with opposite PE polarities. The dephasing effects can be observed in the distorted image obtained directly from the complex PSF data using Eq. 3 (green arrow in Fig. 1E–c). In case of time-invariant off-resonance effects, the PSF in Eq. 1 can be simplified by a single delta function with a phase change (Chung et al., 2011):

$$M(s - y - \Delta B(s)) = \delta(s - y - \Delta B(s)) \exp(ik_{y0} \Delta B(s)), \quad (5)$$

where, k_{y0} is the first phase-encoding line in the EPI-PE dimension. As illustrated by the arrows in Fig. 1E–a, PSFs are aligned with different shifts and phases along the non-distorted direction (s) in the distorted coordinate (y) in severely compressed areas. Thus, integration of the PSFs with different phases yields intra-voxel dephasing effects leading to signal dropouts in the distorted image calculated by Eq. 3. In distinction, these can be avoided if the magnitude of the PSF data is used for the calculation (Fig. 1E–b). This is because the PSFs are located at different positions in the 2D PSF- and EPI-PE space (i.e. an identical position along the distorted coordinate (y), but different locations in the non-distorted coordinate (s)). Therefore, the PSF profiles can still be measured from the GE-PSF data, even in the severely compressed regions (see Fig. 1D) appearing as strong signal dropouts in GE-EPI. The reliable measurements enable geometric correction of the opposite (i.e. stretched) distortions without such dephasing effect in the corresponding GE-EPI pair (Fig. 1F–c and –d) using a kernel calculated from the extended GE-PSF data $I_r(s, y)$ in Eq. 4.

In addition, susceptibility-induced local gradient can lead either a shorter or longer effective TE, resulting in higher and lower image intensity (Figs 1D–c and 1D–d). The signal loss due to the longer effective TE may hinder accurate determination of the PSF profiles from the 3D PSF data measured with one PE polarity, especially in regions with strong susceptibility effects. To minimize the effects, a shorter echo time (TE) for GE-PSF than for GE-EPI sequence is applied in this approach (see arrows in Figs 1E–c vs. 1E–d and 1F–c vs. 1F–d).

It is important to note that the reverse gradient approach adapted in this study is different from the original reverse gradient approaches that have been used in the past (Andersson et al., 2003; Morgan et al., 2004; Meara et al., 2008; Embleton et al., 2010; Holland et al., 2010), in which a reverse EPI is required to estimate the distortion map. In contrast, the PSF approach does not require a reverse gradient PSF scan for this estimation, since information regarding geometric distortion in both the forward and reverse EPIs is calculated from the measured PSF data with one PE direction. The reverse PE gradient EPI is added here to take advantage of the fact that the areas of stretching and compression in GE-EPI and related signal dropouts complement each other in forward and reverse GE-EPI scans.

Experimental validation in phantom

A PSF sequence was implemented based on the product EPI sequence on a 3T Signa Excite MRI scanner (16.0M4, GE Medical Systems, Milwaukee, WI). For the phantom experiment, pairs of PSF and EPI data with opposite PE polarities were acquired using a 8-channel head coil (Invivo Diagnostics, Gainesville, Florida, USA) after a metallic DBS lead extension (Model 37081-60, Medtronic Inc.) had been attached to the surface of the spherical phantom in order to produce metal-induced susceptibility artifacts near the boundaries of the phantom. The imaging protocols were: TR/TE(PSF)/TE(EPI)=2000/30/37 ms, partial Fourier (PSF and EPI)=7/8 and 8/8, parallel imaging acceleration factor=2, 24 slices, matrix size=96×96, image field of view (FOV)=192×192 mm², readout bandwidth=62.5 KHz (equal to 651 Hz/pixel), 2 mm isotropic voxel resolution. The PSF reference acquisition was performed without acceleration and the scan time was 3 minute 12 seconds (TR×segments=2×96) for each PSF data acquisition.

DBS-fMRI in swine

Eleven healthy pigs underwent unilateral nucleus accumbens DBS-fMRI on the same MRI scanner using a homemade 6-channel receive-only surface coil. The details of preoperative imaging and DBS electrode implantation have been described previously (Min et al., 2012; Knight et al., 2013). All procedures followed the National Institutes of Health Guidelines for Animal Research (Guide for the Care and Use of Laboratory Animals) and were approved by the Mayo Clinic Institutional Animal Care and Use Committee (IACUC). An anatomical 3D MPRAGE volume for DBS targeting was acquired with the following imaging protocols: TR/TE =8.06/3.30 ms, inversion time=1000 ms, flip angle=8°, slice thickness=0.8 mm, matrix size=300×300×108, FOV=240×240×87 mm³, and average=2. The scan time was 25 minutes 36 seconds. For electrical stimulation during fMRI scans, a unilateral DBS lead was externalized and connected to an external pulse generator for electrical stimulation (5 Volt, 130 Hz, 100 μsec pulse width, biphasic configuration using the 0(–) and 1(+) contacts of the 3389 lead), which was synchronized to the start time of the fMRI scan. A block paradigm

consisted of 5 rest (30 sec.) and electrical stimulation (6 sec.) cycles and ended with a rest period. The PE polarity in GE-EPI was alternated, which resulted in pairs of GE-EPIs with opposite geometric distortion. The imaging parameters were: TR/TE=1500/40 ms, no partial echo, parallel imaging acceleration factor=2, 19 slices, slice thickness=2.4 mm, readout bandwidth=62.5 KHz, FOV= 160×160, matrix size=96×96, voxel resolution=1.7×1.7×2.4 mm³. To calculate both kernels for distortion correction of the EPI pair with opposite distortions, PSF reference data were acquired in a prior scan using identical imaging parameters with a TE (30 ms) shorter than the one for fMRI to minimize T2* dephasing effects of the PSF. The PE polarity yielding primarily stretched distortions around the DBS electrodes was chosen for the PSF scan.

Image reconstruction and fMRI data analysis

All PSF and fMRI data were reconstructed offline using Matlab (The MathWorks, Inc., USA). PSF reference data with one PE polarity were collected and extended to generate the corresponding PSF data with opposite distortions. Two distortion correction kernels were obtained from the measured and extended PSF reference data in order to correct geometric distortions in the pair of GE-EPIs with opposite distortions. After correcting for distortion, combined images were generated by the square root of the sum of the square of the two distortion-corrected images, which resulted in a combination weighted by the image intensity at that location. This accounts for a residual intensity mismatch between the pair of distortion-corrected GE-EPIs with opposite PE polarities and puts stronger weight on the image with higher signal assuming that this is more sensitive to detect BOLD responses. Therefore, a total of five different variants of the EPI series including forward and reverse phase-encoded EPIs without (NF and NR) and with distortion correction (DF and DR) and the weighted combination of the distortion-corrected EPI pair (DW) were obtained and the total number of time points was reduced by half in all the different EPI series.

The AFNI (Analysis of Functional NeuroImages; <http://afni.nih.nih.gov>) software package (Cox, 1996; Cox and Jesmanowicz, 1999) was used to process the DBS-fMRI data. This includes spike removal (3dDespike), motion correction (3dvolreg), spatial smoothing (3 mm FWHM), and co-registration to the high-resolution pig brain atlas (Saikali et al., 2010) with the cost function of the Hellinger metric (Taneja, 2005). Co-registration between individual EPI datasets and for the high-resolution pig brain atlas (Saikali et al., 2010) was performed based on the non-distorted reference image calculated from the magnitude PSF data, since the image has a high SNR and is geometrically matched with the distortion-corrected EPIs. The transformation matrix was applied to all of the five different variants of EPI series for comparison. A general linear model (GLM) estimation was employed to obtain BOLD signal changes for individuals induced by electrical stimulation. After using the block response model ('BLOCK' in 3dDeconvolve) to estimate hemodynamic response in each individual subject, a one-sample t-test (3dttest) was used for group-level analysis. Furthermore, the signal percentage changes (3Dfim+) of the BOLD time series were additionally calculated from each individual to confirm the corresponding GLM estimation results.

In order to evaluate the improvements associated with the proposed DBS-fMRI approach, the image intensity and BOLD contrasts in the regions with strong susceptibility artifacts was compared visually and quantitatively among the five different variants of the EPI series. Eight subjects among eleven underwent DBS-fMRI experiments for group analysis.

Results

The results of the phantom experiment in Figure 2 present the geometric and intensity distortions caused by the metallic DBS lead extension and the correction using the proposed approach. Both strong image compression and stretching near the metallic DBS lead and connector were clearly seen in the distorted forward (NF) and reverse EPIs (NR). Strong signal dropouts could be visualized in the strongly compressed areas after geometric distortion correction (DF and DR). Since stretched distortions were more dominant in the acquisition of reverse EPI, the intensity distortions were less after geometric distortion correction (DR). The decrease in intensity distortions was approximately 60.7% (DR in B). Using the proposed approach, it was possible to further reduce the intensity distortions up to 83.1% (DW in B).

Figure 3 shows the correction fidelity of the proposed approach around the implanted DBS electrode in the pig brain. Due to the different patterns of signal dropouts between the distortion-corrected EPI pair (DF and DR), the loss of spatial information around the DBS electrode was partially recovered after the weighted combination (DW). Quantitative evaluations of the advantage of combining the image pair (light gray in 3B–b) over choosing an optimal PE polarity (dark gray in 3B–b) around the metallic electrode in the brain (Fig. 3B) show signal recoveries of $23.9\pm 17.3\%$ and $40\pm 11.0\%$, respectively. The difference in signal recovery was statistically significant (paired t-test, p -value=0.001). Among the 11 subjects, less intensity distortions in either the forward or reverse phase-encoded EPIs were observed for 5 and 6 subjects, respectively. Therefore, there was no preferred PE polarity that could minimize the intensity distortions around the metallic electrode.

As shown in Figure 4, due to metal-induced susceptibility effects around the metallic electrode, a strong loss of signal intensity occurs in both the distortion-corrected forward (DF) and the reverse EPI (DF), resulting in loss of BOLD contrast in the affected areas. The local differences in image intensity and the BOLD contrasts between the image pair were well-preserved in the combined EPI (see arrows). In addition, the volume of activation cluster was further increased due to the improved SNR in the final image series (DW) after combining the distortion-corrected forward and reverse EPI series (DF and DR).

Figure 5 shows that this approach is also beneficial in terms of improving the BOLD contrast near tissue-air boundaries. As shown in the coronal and sagittal images from the anatomical MPRAGE acquisition (A), large frontal sinus cavities are often present near the frontal lobe of the pig brain. Consequently, strong susceptibility artifacts appeared in the form of either strong compressed (DF in B) or stretched distortions (DR in B) in the corresponding regions. With the fixed image orientation (orange-colored stick in A), more prominent image compressions in the forward EPI and dominant intensity distortions in the distortion-corrected forward EPI (DF in B) were measured near the frontal lobe of the pig

brain. In contrast to metal-induced susceptibility artifacts, however, the loss of signal intensity and BOLD contrast near tissue/air boundaries were nearly fully resolved when the proposed approach was used (DW in B).

Figure 7 shows that the proposed approach can improve the local BOLD contrast in the group activation map. As shown in the BOLD contrasts in the axial (B) and sagittal slices (C), the volume in the group activation map was increased overall after geometric distortion correction for data for each individual resulting in good geometric agreement of local activations between subjects, as shown in both the forward (NF vs. DF) and reverse EPIs (NR vs. DR). However, the group BOLD contrasts in between the distortion-corrected EPIs were not geometrically matched well, especially in the frontal and subcortical regions (see green and blue arrows), as observed in each individual data (Figs. 4, 5, and 6). After combining the distortion-corrected EPI pair, the overall BOLD activations from both the distortion-corrected forward (DF) and reverse EPIs (DR) were found in the final group map (DW).

Figure 8 shows a quantitative evaluation of the increase in BOLD activation from group data in the subcortical (B-a), the frontal (B-b), and the entire brain areas (B-c). Although the size of the activation volume was increased and the statistical significance was improved after combining the distortion-corrected EPI pair in all regions (DW), the main contributions to the improvements between the distortion-corrected EPIs were significantly different in local areas. In the subcortical mask areas (B-a), significant increase in the size of the activation volume was found in the forward EPI after distortion correction (NF vs. DF in B-a) while the statistical significance was improved both in the forward and reverse EPIs. In contrast, improvements were observed only in the reverse EPI after distortion correction in the frontal mask area (NR vs. DR in B-b). When considering the entire brain volume, however, no prominent PE polarity was found for the improvements in BOLD activation after distortion correction (B-c). In addition, the main contributions in increasing the activation volume size were achieved mostly in the lower range of statistical significance in the entire brain volume (DW in B-c), but in the higher ranges of statistical significance in the subcortical (DW in B-a) and frontal mask areas (DW in B-b).

Discussion

In this study, we adapted the PSF mapping-based reversed gradient approach for DBS-fMRI applications, investigated a theoretical background depicting the applicability to GE-EPI, and evaluated the efficiency in minimizing metal-induced susceptibility artifacts as well as susceptibility artifacts in the regions near tissue/air boundaries. To evaluate the performance of this approach, NAc DBS-fMRI was carried out in swine and the improvements in recovering local losses of image intensity and BOLD contrasts by electrical stimulation were evaluated visually and quantitatively in each individual and for the entire group. Due to the different patterns of local signal dropouts in the pair of GE-EPIs with opposite distortions, combining the distortion-corrected pair permitted intensity loss to be partially recovered and thus, the loss of local activation in the final image. The improvements in individual data resulted in an apparent BOLD contrast being obtained from the group data in the areas suffering from severe susceptibility artifacts.

Although the efficiency of this approach adapted for DBS-fMRI was evaluated in swine at 3T, we expect its application in human subjects will yield similar results. As demonstrated by the results from in-vivo pig and phantom experiments, this approach permits metal-induced susceptibility artifacts to be minimized both around the DBS electrode and near the DBS lead and the connector. In addition, susceptibility artifacts in the regions near tissue/air boundaries such as the frontal and temporal lobes of the human brain can be resolved efficiently using the proposed approach. Furthermore, the issue of the safety of patients with DBS implants is recognized as important. As shown in phantom (Carmichael et al., 2007; Gorny et al., 2013), *in-vivo* animal experiments (Gorny et al., 2013), and *in-vivo* human studies (Sammartino et al., 2016), the use of DBS-fMRI using GE-EPI would be expected to be safe, even at 3T. The GE-PSF mapping sequence is identical to the GE-EPI sequence, except for an additional PSF-PE gradient. Since the heating effects of the DBS electrode contacts are mainly induced by the applied RF power rather than the gradient, no significant changes in heating would be expected in a GE-PSF scan compared to GE-EPI. Therefore, this approach could allow reliable DBS-fMRI studies to be conducted in patients with an acceptable level of safety. Nevertheless, MR safety for a PSF scan needs to be confirmed before applying this approach to human DBS-fMRI studies.

A previous study (Embleton et al., 2010) reported that the conventional reverse gradient approach based on SE-EPI could also be useful for fMRI since SE-EPI does not suffer from signal dropout caused by image compression in the acquired image. However, this may not be suitable for DBS-fMRI, due to the very conservative SAR-limitations associated with the use of a DBS electrode. The use of a refocusing RF pulse leads to a significant increase in SAR and could result in a higher temperature increase at the DBS electrode contacts during DBS-fMRI scans. Compared to GE-EPI, heating effects that were more than three times higher were observed in a previous study (Georgi et al., 2004). Alternatively, a pair of SE-EPIs with opposite PE polarities could be measured separately to calculate geometric distortions in the corresponding pair of GE-EPIs with opposite distortions to be applied for fMRI (Holland et al., 2010). However, the application might still be limited due to the rapid heating effects at the DBS electrode contacts, where 80% of the total temperature increase occurred during the first 30s after the start of the acquisition (Georgi et al., 2004; Gorny et al., 2013). In addition, accurate distortion information cannot be calculated only from the SE-EPI pair with opposite distortions in severely warped regions (In et al., 2015), such as areas around/near the metallic DBS devices. Even though there may be no SAR issues related to measuring the corresponding distortion information using both the conventional field mapping (Jezzard and Balaban, 1995) and the original PSF mapping methods (Zaitsev et al., 2004), there is still a limitation in reliably correcting for severe distortions, as previously reported in studies conducted at 7T (Chung et al., 2011; In, 2012). In contrast, the correction fidelity of the proposed approach was well demonstrated in previous studies (In and Speck, 2012; In et al., 2015) and in this study. Therefore, the proposed approach would be a viable method for considering both SAR concerns and the correction fidelity in performing DBS-fMRI studies.

It should be noted that the proposed approach cannot correct for through-plane spin dephasing and thus image intensity loss due to very strong susceptibility-induced local gradients in the slice direction arising from metallic DBS devices. As shown in Fig. 3A,

there are still losses of signal around the DBS electrode, even in the reference image without geometric distortion. The effect of the local gradient in the slice direction can be mitigated only with a compensation gradient with opposite polarity on the slice selection axis, which is the basic principle of z-shimming (Frahm et al., 1988). However, the compensation gradient will not correct for the effects of in-plane susceptibility-induced gradients (Deichmann et al., 2002).

Signal dropout in GE-EPI caused by intravoxel dephasing effects due to severe image compression could be mainly recovered with the proposed approach. Nevertheless, substantial improvements of up to 83.1 and 40%, respectively, were achieved near the DBS lead (Fig. 2) and around the DBS electrode (Fig. 3). In contrast to the group activation results from a previous NAc DBS-fMRI study (Knight et al., 2013), subcortical activations near the regions of the DBS electrode tip were clearly observed in this study (Fig. 7), which is in agreement with observations reported in previous human studies (Rauch et al., 2006; Bewernick et al., 2010; Gibson et al., 2016a). Therefore, the improvements associated with the proposed approach would still be meaningful in terms of studies related to DBS mechanisms.

The improvements in local BOLD contrasts arising from the improved signal redistribution and the increased image SNR after image combination may not be clearly distinguished using only the statistically significant BOLD effects, as shown in Figs. 4 and 5. To demonstrate that the main improvements were in the local BOLD contrasts, the corresponding percentage signal changes were calculated. In contrast to the GLM-based BOLD signal changes, the SNR does not play a significant role in calculating the percent signal change since the signal baseline and the number of stimulation blocks are identical in all of the distortion-corrected forward (DF), the reverse (DR), and combined data (DW). Therefore, the increases in the local activation volume, which were observed in both the GLM ($p < 0.001$) BOLD effect maps (Figs. 4 and 5) and the high (>1%) signal percentage change maps (Fig. 6), are likely arising from the improved signal redistribution after image combination.

Extending the hypothesis from the previous NAc DBS-fMRI study (Knight et al., 2013), this study provides evidence that the accurate correction of local susceptibility artifacts from the DBS leads is very important to enable detection of the local BOLD contrast in subcortical areas from data for an entire group. Different degrees of local geometric distortions in data for each individual could cause a mismatch of local activations between subjects and could result in the absence of any significant activation in the affected areas. While the cluster size of the activation volume was very small without geometric distortion correction, together with a lower level of statistical significance, these were substantially improved after distortion correction in both subcortical (NF vs. DF in Figs. 7 and 8) and frontal areas (NR vs. DR in Figs. 7 and 8). When intensity distortions were dominant in the acquired image, however, the loss of BOLD activation in the subcortical (NR vs. DR in Figs. 7 and 8) and frontal areas (NF vs. DF in Figs. 7 and 8) could not be recovered, even with accurate geometric distortion correction. Since the local activation losses were considerably different with changes in PE polarity, the local variations across subjects could be minimized in the final image after combination of the distortion-corrected image pair. As a result, the size of

the activation volume in higher ranges of statistical significance was increased more notably in the group map in the subcortical (DW in Fig. 8B–a) and frontal areas (DW in Fig. 8B–b). Due to the SNR improvement in the combined image, however, the activation volume size was increased mainly in the lower range of statistical significance over the entire brain volume (DW in Fig. 8B–c). In other words, the higher SNR obtained by either higher temporal resolution or image average cannot lead to the improvements observed with the proposed approach in the local areas. Therefore, the proposed method for a reverse gradient approach can be very beneficial in terms of minimizing the loss of local BOLD activation according to the PE dependency.

There are several challenges for this approach to be more efficient for DBS-fMRI application. First, a theoretical background study (Embleton et al., 2010) should be considered and investigated further to optimally combine distortion-corrected image pairs. In this work, based on the assumption that a higher image SNR is more sensitive for detecting BOLD responses, the distortion-corrected images were combined by the sum-of-squares method as a weighted combination scaled by the image intensity. This may not be optimal, especially in regions with strong susceptibility effects due to variations in the effective TE resulting in different local BOLD sensitivities. However, the Nac DBS-fMRI performed in this study is appropriate for evaluating the improvements in recovering local losses of image intensity and BOLD contrasts by combining distortion-corrected image pairs, but not for searching for the optimal route to maximize the improvements. Since there were some delays and latencies of the hemodynamic response function for electrical stimulation (Min et al., 2012; Knight et al., 2013; Min et al., 2014; Ross et al., 2016), the temporal structure should be investigated in more detail in order to more accurately interpret the functional activation data, which would enable a search for the optimal route for combining the distortion-corrected image pair.

Finally, intensity distortions were minimized in this approach at the cost of reduced temporal resolution by a factor of 2, due to the interleaved acquisition of the EPI pair series with opposite PE polarities during the DBS-fMRI scan (i.e. 1.5 sec. per each EPI volume, but 3 sec. per each DW volume in this study). As a future development, multi-echo EPI combined with a reverse gradient approach (Weiskopf et al., 2005), which acquires two or more sequential echoes with opposite PE polarities, will be considered in order to speed up this approach. Although multi-band approaches (Moeller et al., 2010; Setsompop et al., 2012) can offer a great benefit to increase the temporal resolution, their application to fMRI during DBS stimulation may require further investigation due to the use of the multi-band RF pulses, which lead to high SAR.

Conclusion

In this study, we adapted a PSF mapping-based reverse gradient approach for DBS-fMRI in swine, in an attempt to minimize susceptibility artifacts and investigate the efficiency and reliability of DBS-fMRI studies. The results demonstrate that the proposed approach permits geometric distortions of GE-EPI data with reversed PE directions to be corrected efficiently and strong susceptibility artifacts around the metallic electrodes to be minimized, as well as in the regions near tissue/air boundaries in the brain. Therefore, the proposed approach

represents a viable method for improving BOLD contrast for DBS-fMRI, which will be beneficial in terms of investigating the mechanisms responsible for DBS.

Acknowledgments

This work was supported by The Grainger Foundation and by the National Institutes of Health (R01 NS 70872 awarded to K.H.L.). We are grateful to Dr Milton S. Feather for tidying up English grammar and expression in this manuscript.

References

- Andersson JL, Skare S, Ashburner J. How to correct susceptibility distortions in spin-echo echo-planar images: application to diffusion tensor imaging. *Neuroimage*. 2003; 20:870–888. [PubMed: 14568458]
- Bewernick BH, Hurlmann R, Matusch A, Kayser S, Grubert C, Hadrysiewicz B, Axmacher N, Lemke M, Cooper-Mahkorn D, Cohen MX. Nucleus accumbens deep brain stimulation decreases ratings of depression and anxiety in treatment-resistant depression. *Biological psychiatry*. 2010; 67:110–116. [PubMed: 19914605]
- Carmichael DW, Pinto S, Limousin-Dowsey P, Thobois S, Allen PJ, Lemieux L, Yousry T, Thornton JS. Functional MRI with active, fully implanted, deep brain stimulation systems: safety and experimental confounds. *Neuroimage*. 2007; 37:508–517. [PubMed: 17590355]
- Chung JY, In MH, Oh SH, Zaitsev M, Speck O, Cho ZH. An improved PSF mapping method for EPI distortion correction in human brain at ultra high field (7.0 T). *Magn Reson Mater Phy*. 2011; 24:179–190.
- Cox RW. AFNI: software for analysis and visualization of functional magnetic resonance neuroimages. *Computers and Biomedical research*. 1996; 29:162–173. [PubMed: 8812068]
- Cox RW, Jesmanowicz A. Real-time 3D image registration for functional MRI. *Magnetic resonance in medicine*. 1999; 42:1014–1018. [PubMed: 10571921]
- Deichmann R, Josephs O, Hutton C, Corfield D, Turner R. Compensation of susceptibility-induced BOLD sensitivity losses in echo-planar fMRI imaging. *Neuroimage*. 2002; 15:120–135. [PubMed: 11771980]
- Embleton KV, Haroon HA, Morris DM, Ralph MAL, Parker GJ. Distortion correction for diffusion-weighted MRI tractography and fMRI in the temporal lobes. *Hum Brain Mapp*. 2010; 31:1570–1587. [PubMed: 20143387]
- Frahm J, Merboldt KD, Hänicke W. Direct FLASH MR imaging of magnetic field inhomogeneities by gradient compensation. *Magnetic resonance in medicine*. 1988; 6:474–480. [PubMed: 3380007]
- Georgi JC, Stippich C, Tronnier V, Heiland S. Active deep brain stimulation during MRI: a feasibility study. *Magnetic resonance in medicine*. 2004; 51:380–388. [PubMed: 14755664]
- Gibson WS, Cho S, Abulseoud OA, Gorny KR, Felmlee JP, Welker KM, Klassen BT, Min HK, Lee KH. The impact of mirth-inducing ventral striatal deep brain stimulation on functional and effective connectivity. *Cerebral Cortex*. 2016a bhw074.
- Gibson WS, Ross EK, Han SR, Van Gompel JJ, Min HK, Lee KH. Anterior thalamic deep brain stimulation: Functional activation patterns in a large animal model. *Brain stimulation*. 2016b
- Gorny KR, Presti MF, Goerss SJ, Hwang SC, Jang DP, Kim I, Min HK, Shu Y, Favazza CP, Lee KH. Measurements of RF heating during 3.0-T MRI of a pig implanted with deep brain stimulator. *Magnetic resonance imaging*. 2013; 31:783–788. [PubMed: 23228310]
- Holland D, Kuperman JM, Dale AM. Efficient correction of inhomogeneous static magnetic field-induced distortion in echo planar imaging. *Neuroimage*. 2010; 50:175. [PubMed: 19944768]
- In, MH. Magdeburg, Univ, Fak für Naturwiss, Diss. Magdeburg: Universitätsbibl; 2012. Geometric Distortion Correction in EPI at Ultra High Field.
- In MH, Posnansky O, Beall EB, Lowe MJ, Speck O. Distortion correction in EPI using an extended PSF method with a reversed phase gradient approach. *PLoS ONE*. 2015; 10:e0116320. doi: 0116310.0111371/journal.pone.0116320. [PubMed: 25707006]

- In MH, Speck O. Highly accelerated PSF-mapping for EPI distortion correction with improved fidelity. *Magn Reson Mater Phy*. 2012; 25:183–192.
- Jezzard P, Balaban RS. Correction for geometric distortion in echo planar images from B0 field variations. *Magn Reson Med*. 1995; 34:65–73. [PubMed: 7674900]
- Kim JP, Min HK, Knight EJ, Duffy PS, Abulseoud OA, Marsh MP, Kelsey K, Blaha CD, Bennet KE, Frye MA. Centromedian-parafascicular deep brain stimulation induces differential functional inhibition of the motor, associative, and limbic circuits in large animals. *Biological psychiatry*. 2013; 74:917–926. [PubMed: 23993641]
- Knight EJ, Min HK, Hwang SC, Marsh MP, Paek S, Kim I, Felmlee JP, Abulseoud OA, Bennet KE, Frye MA. Nucleus accumbens deep brain stimulation results in insula and prefrontal activation: a large animal fMRI study. *PLoS ONE*. 2013; 8:e56640. [PubMed: 23441210]
- Meara SJ, Embleton KV, Parker GJ. Distortion correction for a double inversion-recovery sequence with an echo-planar imaging readout. *Magn Reson Imaging*. 2008; 26:943–953. [PubMed: 18524526]
- Min HK, Hwang SC, Marsh MP, Kim I, Knight E, Striemer B, Felmlee JP, Welker KM, Blaha CD, Chang SY. Deep brain stimulation induces BOLD activation in motor and non-motor networks: an fMRI comparison study of STN and EN/GPi DBS in large animals. *Neuroimage*. 2012; 63:1408–1420. [PubMed: 22967832]
- Min HK, Ross EK, Lee KH, Dennis K, Han SR, Jeong JH, Marsh MP, Striemer B, Felmlee JP, Lujan JL. Subthalamic nucleus deep brain stimulation induces motor network BOLD activation: use of a high precision MRI guided stereotactic system for nonhuman primates. *Brain stimulation*. 2014; 7:603–607. [PubMed: 24933029]
- Moeller S, Yacoub E, Olman CA, Auerbach E, Strupp J, Harel N, Urbil K. Multiband multislice GE-EPI at 7 tesla, with 16-fold acceleration using partial parallel imaging with application to high spatial and temporal whole-brain fMRI. *Magn Reson Med*. 2010; 63:1144–1153. [PubMed: 20432285]
- Morgan PS, Bowtell RW, McIntyre DJ, Worthington BS. Correction of spatial distortion in EPI due to inhomogeneous static magnetic fields using the reversed gradient method. *J Magn Reson Imaging*. 2004; 19:499–507. [PubMed: 15065175]
- Rauch SL, Dougherty DD, Malone D, Rezai A, Friehs G, Fischman AJ, Alpert NM, Haber SN, Stypulkowski PH, Rise MT. A functional neuroimaging investigation of deep brain stimulation in patients with obsessive-compulsive disorder. *Journal of Neurosurgery*. 2006; 104:558–565. [PubMed: 16619660]
- Robson MD, Gore JC, Constable RT. Measurement of the point spread function in MRI using constant time imaging. *Magn Reson Med*. 1997; 38:733–740. [PubMed: 9358447]
- Ross EK, Kim JP, Settell ML, Han SR, Blaha CD, Min HK, Lee KH. Fornix deep brain stimulation circuit effect is dependent on major excitatory transmission via the nucleus accumbens. *Neuroimage*. 2016; 128:138–148. [PubMed: 26780572]
- Saikali S, Meurice P, Sauleau P, Eliat PA, Bellaud P, Randuineau G, Verin M, Malbert CH. A three-dimensional digital segmented and deformable brain atlas of the domestic pig. *J Neurosci Methods*. 2010; 192:102–109. [PubMed: 20692291]
- Sammartino F, Krishna V, Sankar T, Fisico J, Kalia SK, Hodaie M, Kucharczyk W, Mikulis DJ, Crawley A, Lozano AM. 3-Tesla MRI in patients with fully implanted deep brain stimulation devices: a preliminary study in 10 patients. *Journal of Neurosurgery*. 2016:1–7.
- Setsompop K, Gagoski BA, Polimeni JR, Witzel T, Wedeen VJ, Wald LL. Blipped-controlled aliasing in parallel imaging for simultaneous multislice echo planar imaging with reduced g-factor penalty. *Magn Reson Med*. 2012; 67:1210–1224. [PubMed: 21858868]
- Taneja I. Refinement inequalities among symmetric divergence measures. *The Australian Journal of Mathematical Analysis and Applications*. 2005; 2:1–23.
- Weiskopf N, Klose U, Birbaumer N, Mathiak K. Single-shot compensation of image distortions and BOLD contrast optimization using multi-echo EPI for real-time fMRI. *Neuroimage*. 2005; 24:1068–1079. [PubMed: 15670684]

Zaitsev M, Hennig J, Speck O. Point spread function mapping with parallel imaging techniques and high acceleration factors: Fast, robust, and flexible method for echo planar imaging distortion correction. *Magn Reson Med.* 2004; 52:1156–1166. [PubMed: 15508146]

Author Manuscript

Author Manuscript

Author Manuscript

Author Manuscript

Highlights

- PSF mapping-based reverse gradient approach can be adapted to minimize susceptibility artifacts in fMRI
- This approach can minimize susceptibility artifacts that appear around the metallic electrodes
- Susceptibility artifacts near the tissue/air boundaries in the brain can also be resolved
- With the distortions minimized, local BOLD contrast in DBS-fMRI can be improved

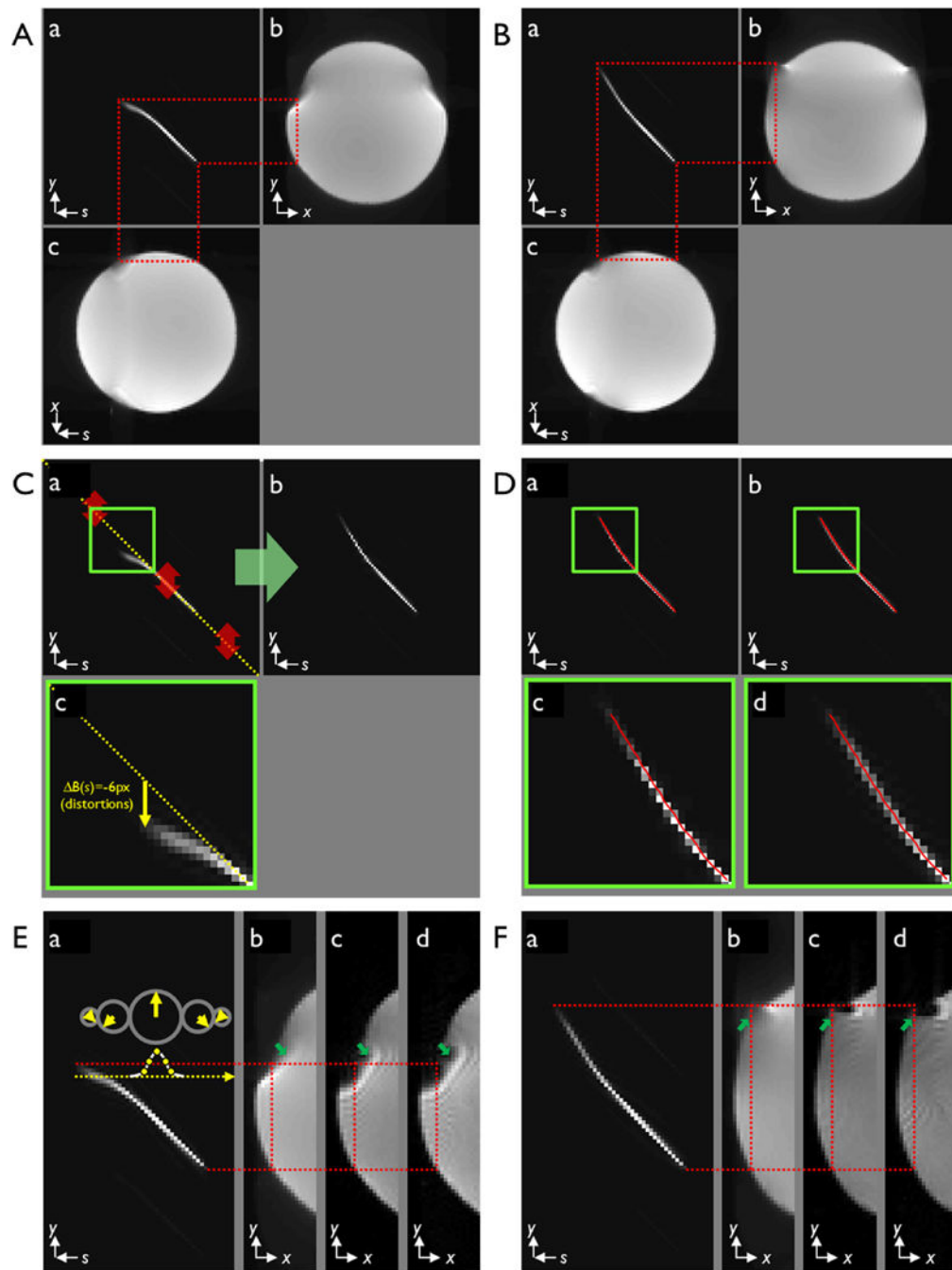


Figure 1.

Comparison of geometric distortions in a pair of forward (A) and reverse GE-PSF data (B): a 2D PSF image in s - y plane at $x=15$ (a), distorted (b) and non-distorted reference images (c) calculated by Eqs. 3 and 2 from the magnitude 3D GE-PSF data, respectively; (C-a) procedure of inversion of the 2D PSF image from (A-a) by Eq. 4, (C-b) corresponding mirrored 2D PSF image, and (C-c) an expansion image from a small portion of the 2D PSF image in (C-a); (D) comparison between two 2D PSF images, mirrored from the forward 2D PSF image (D-a) and measured reverse 2D PSF image (D-b). Expansion images (D-c and

D–d), respectively from a small portion of the 2D PSF image in (D–a and D–b). Red lines overlaid on all images in (D) demonstrate the center position of PSF along the y-direction in the s-coordinates; Differences of intra-voxel dephasing effects in the compressed (E) and stretched areas (F): distorted images calculated from the magnitude (b) and complex (c) PSF data by Eq. 3 and corresponding GE-EPI acquired with a longer TE (d).

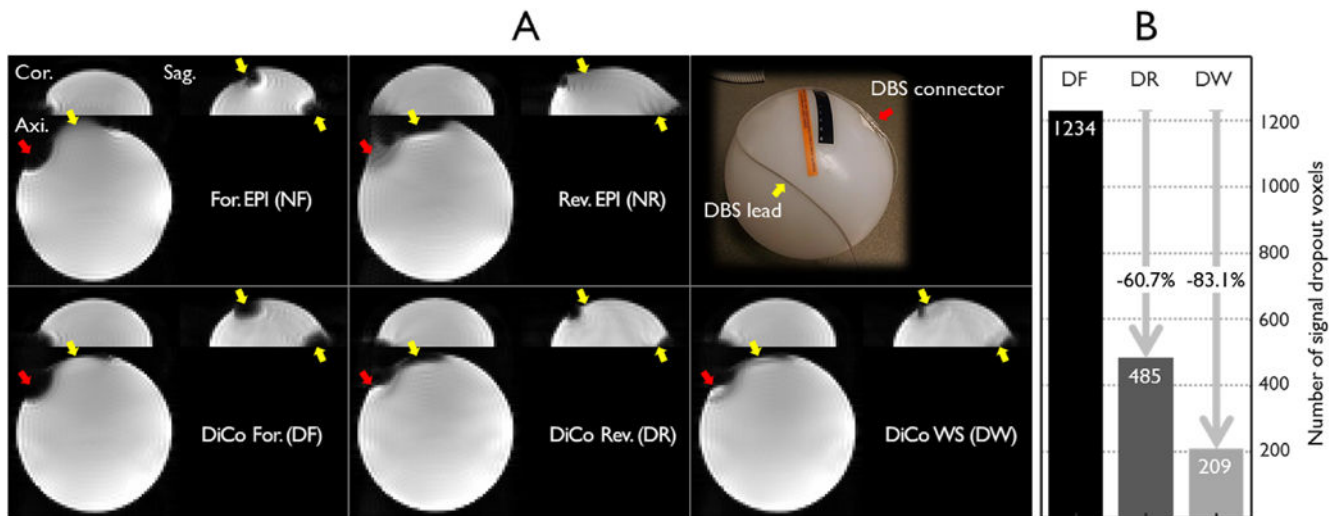


Figure 2.

Correction fidelity in minimizing geometric and intensity distortions near the metallic DBS connector and the lead in phantom (A) and the quantitative evaluation for signal recovery performance (B). In (A), forward and reverse EPI without (NF and NR) and with distortion correction (DF and DR) and the weighted average of the distortion-corrected image pair (DW) are shown, in addition to the picture of the phantom attached with DBS connector and the lead (right and top in A). coronal (Cor.), sagittal (Sag.), and axial (Axi.) images were chosen for demonstration. Arrows indicate geometric and intensity distortions near the DBS connector (red) and lead (yellow) in forward (NF) and reverse EPIs (NR), geometric distortion correction in the distortion-corrected forward (DF) and reverse EPIs (DR), and corresponding signal recovery in the combined image (DW). In (B), intensity distortions in the distortion-corrected forward (DF), the reverse (DR), and the combined EPIs (DW) are shown, as the total number of signal dropout voxels counted in the areas with signal intensity less than a threshold value (half of the averaged magnitude value of the phantom image).

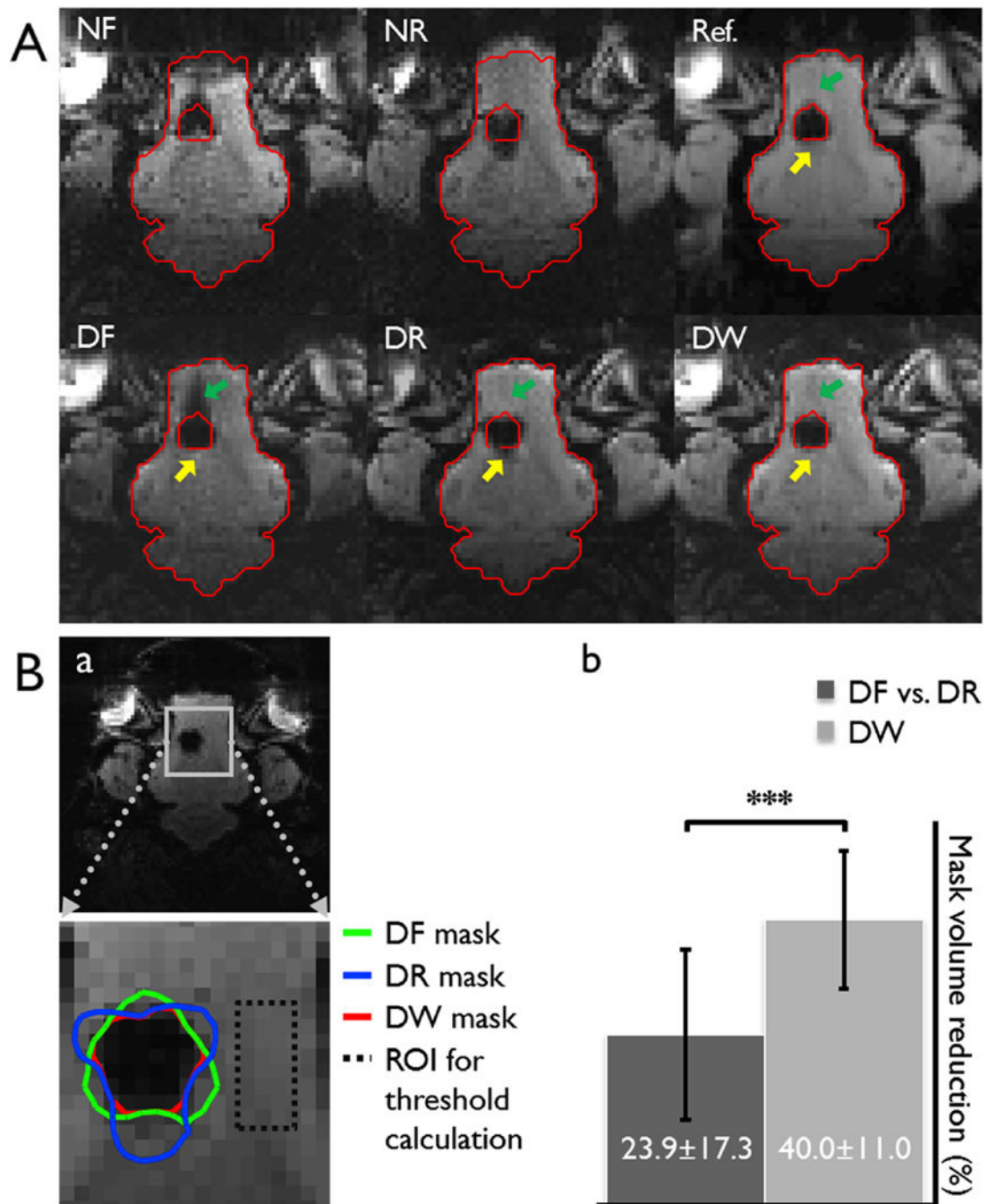


Figure 3. Correction fidelity of the proposed approach (A) and the quantitative evaluation of intensity distortions around the metallic electrode in the pig brain (B). In (A), forward and reverse EPI with (NF and NR) and without distortion correction (DF and DR) and the weighted average of the distortion-corrected image pair (DW) in an in-vivo pig brain with an implanted DBS electrode are shown. The red-contours of the pig brain calculated from the non-distorted reference (Ref.) image were overlaid on all images in (A) to present the correction fidelity more clearly. Green and yellow arrows indicate signal dropouts in forward and reverse

distortion-corrected EPIs, respectively and demonstrate the signal recovery in corresponding areas of the combined image (DW). In (B–a), image masks of the distortion-corrected forward (DF), reverse (DR), and the combined EPIs (DW) in the areas of signal dropout, where the signal intensity is less than a threshold value (half of the averaged magnitude value in a region of interest (ROI)), are presented as color contours. As ratios, the mask volume reductions (i.e. signal recoveries) obtained by choosing an optimal PE polarity (dark gray) and by combining the image pair (light gray) are shown in (B–b) and the difference is statistically significant (paired sample t-test, $p < 0.001$). Datasets from eleven different subjects were used for the calculation.

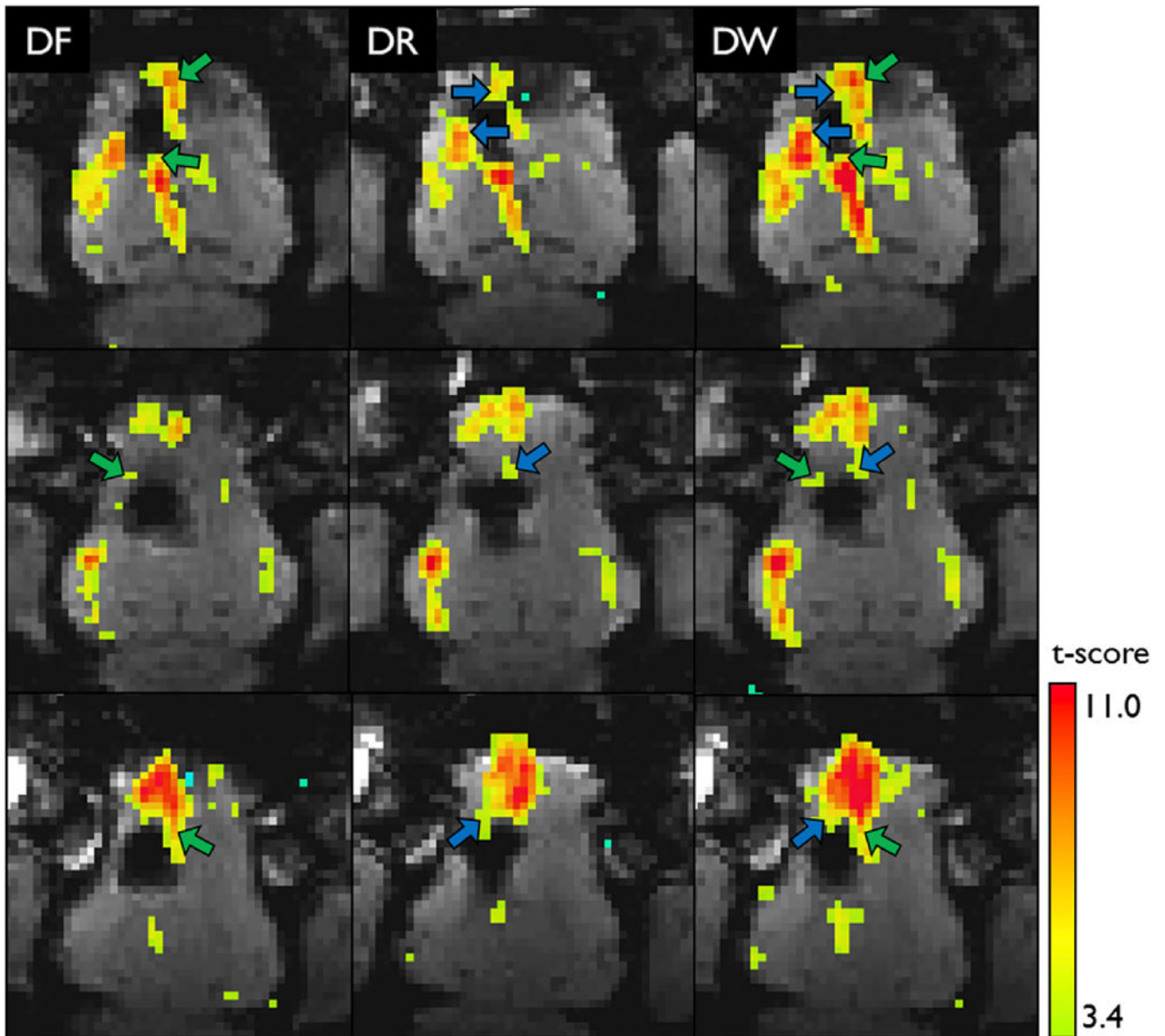


Figure 4. BOLD contrasts for DBS stimulation effects close to the metallic electrode calculated from forward (DF) and reverse EPI with distortion correction (DR) and the weighted average (DW), and overlaid onto the corresponding EPI images. For demonstration, a slice from three different subjects (from 1st to 3rd row) is chosen. Green and blue arrows indicate BOLD contrasts shown only in the forward or reverse EPIs, respectively. The overlaid color presents the activation at a threshold level $p < 0.001$ ($t\text{-score} > 3.377$, $q\text{FDR} < 0.05$).

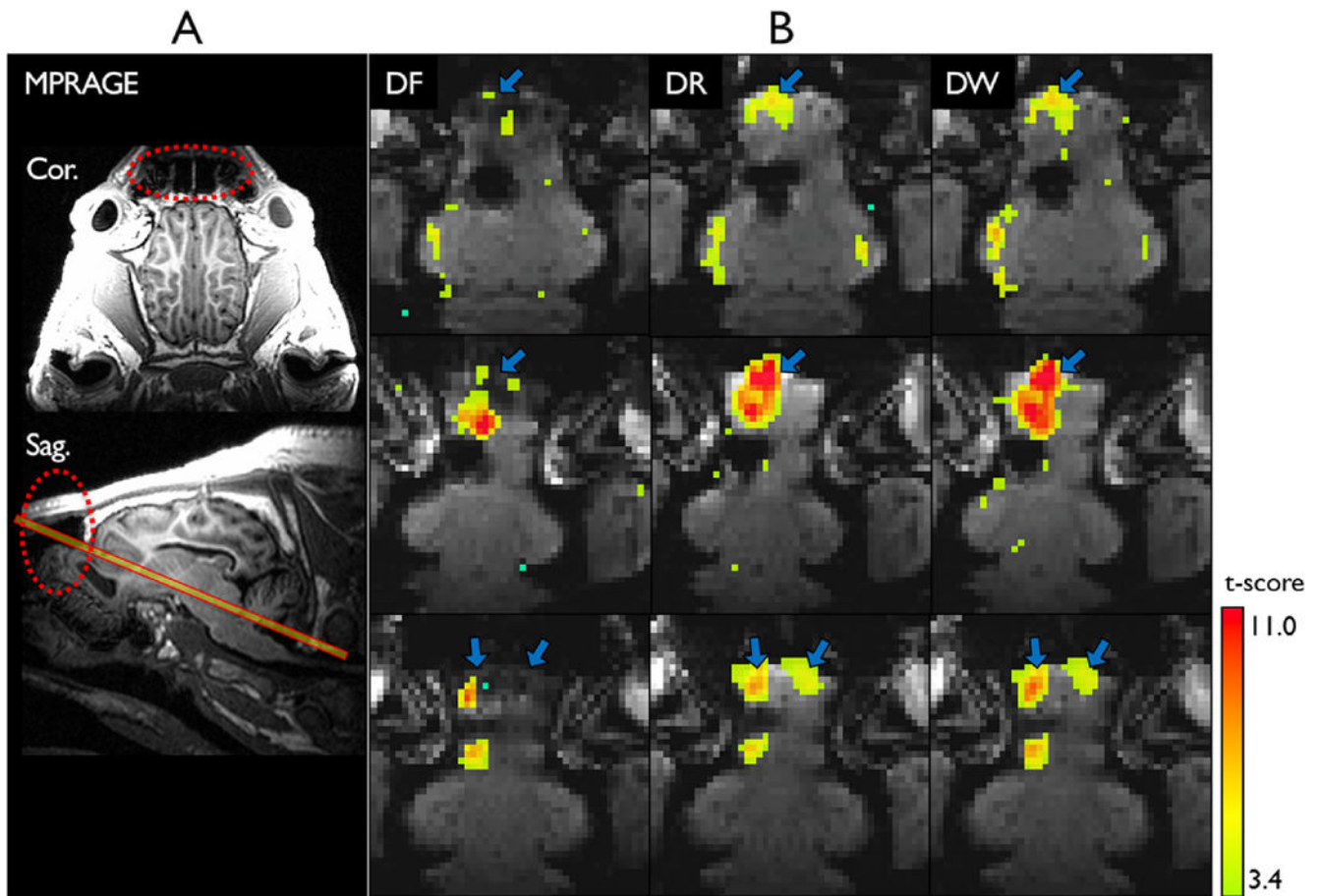


Figure 5. BOLD contrasts for DBS stimulation effects near tissue/air boundaries. (A) Coronal (Cor.) and sagittal (Sag.) images from anatomical MPRAGE acquisition show signal dropout near the frontal lobes of the pig brain, where strong susceptibility effects typically appear. (B) BOLD contrasts calculated from the forward (DF), reverse EPI with distortion correction (DR), and the weighted average (DW) are overlaid over the corresponding EPI data and blue arrows indicate the differences between forward and reverse EPI with distortion correction due to different intensity distortions. For demonstration, a slice from three different subject data (from 1st to 3rd row) is chosen. The overlaid color presents the activation at a threshold level $p < 0.001$ ($t\text{-score} > 3.377$, $q\text{FDR} < 0.05$).

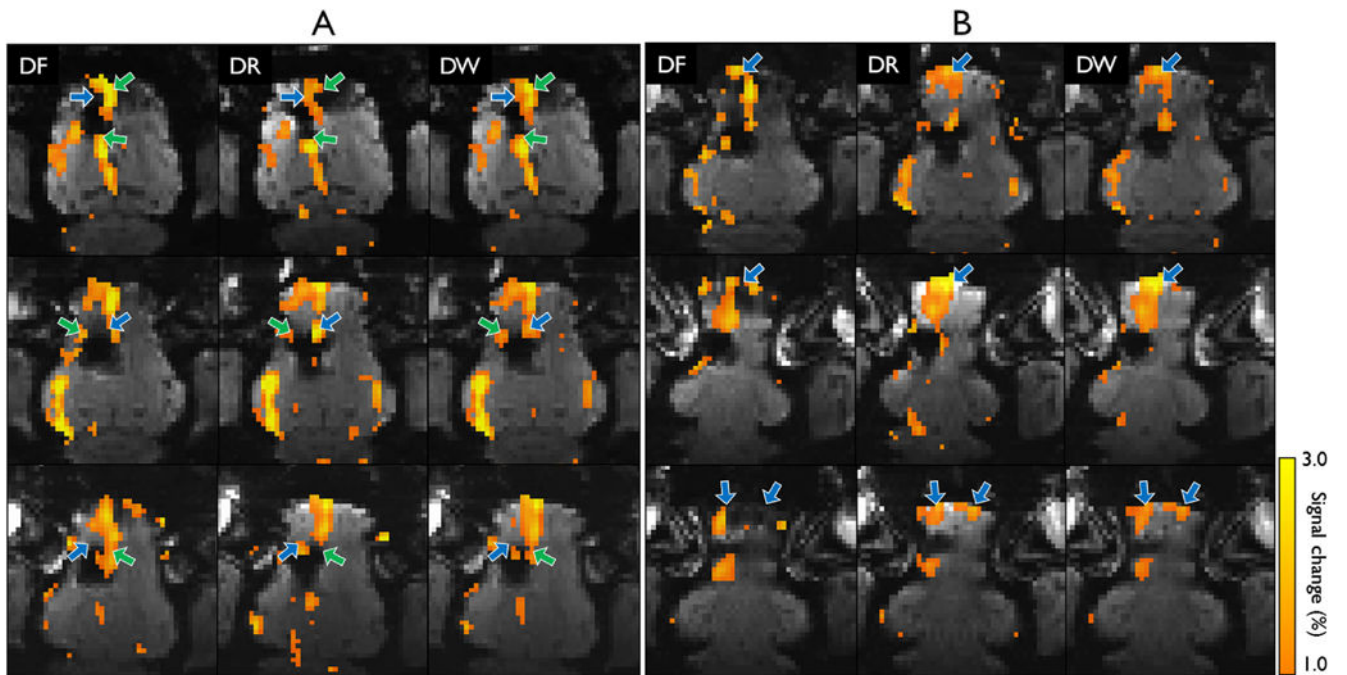


Figure 6. Percentage signal change for DBS stimulation effects close to the metallic electrode (A) and near tissue/air boundaries (B), which correspond to the results of Figs 4 and 5, respectively. The overlaid color presents the percentage change in the signal at a threshold level of 1%.

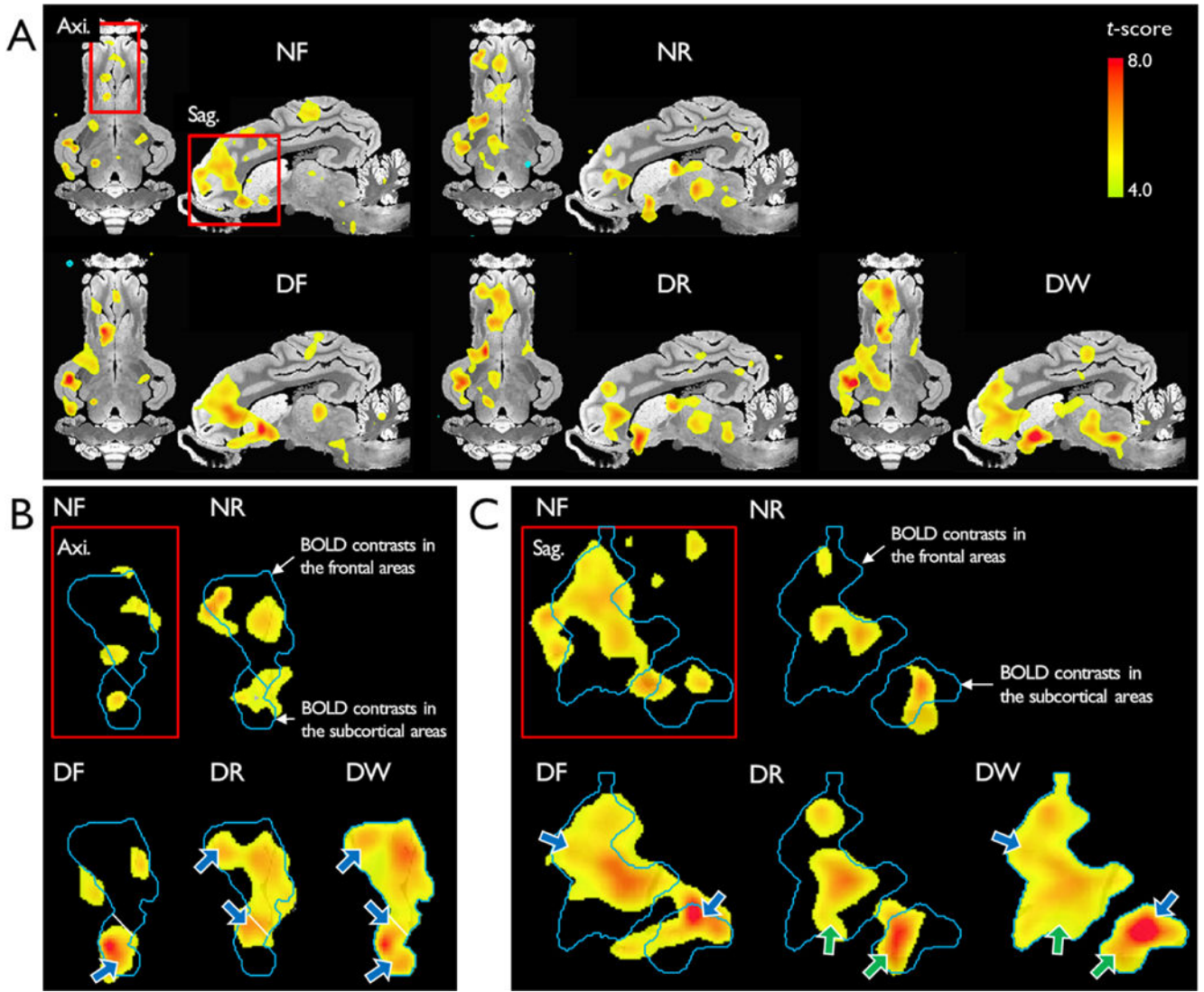


Figure 7. Comparison of group BOLD activation maps from five different variants of the EPI series, forward and reverse EPIs without (NF and NR) and with distortion correction (DF and DR) and the combined EPI for the distortion-corrected EPI pair (DW). The contrasts for the BOLD group were overlaid over the axial and sagittal sections of anatomical brain images (A). For comparison of the BOLD contrasts from the five different variants, a small portion of the BOLD contrasts in the axial (B) and sagittal slices (C) were enlarged. In (B) and (C), blue and green arrows indicate the BOLD contrasts shown only in distortion-corrected forward and reverse EPI, respectively. Green contours calculated from the BOLD contrasts in the combined EPI (DW) are overlaid over all of the BOLD contrasts calculated from all of different EPI variants. The overlaid color presents the activation at a threshold level $p < 0.005$ ($t\text{-score} > 4.029$, $qFDR < 0.05$).

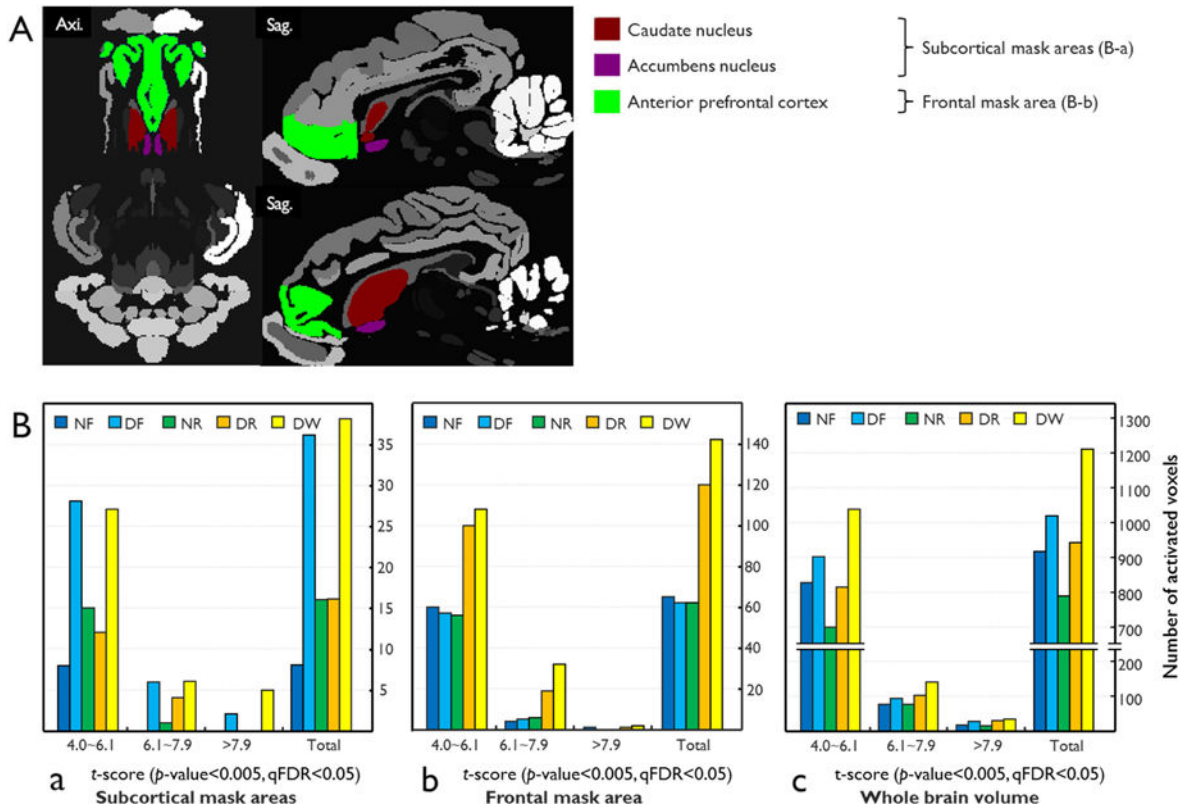


Figure 8.

Quantitative evaluation of pig atlas masks (A) and the number of activated voxels for the BOLD group activation map in the subcortical mask areas (B-a), the frontal mask area (B-b), and the entire brain volume (B-c). As colors, masks of subcortical and frontal areas are shown in (A). Four different variants including forward and reverse EPIs without (NF and NR) and with distortion correction (DF and DR), and the combined image of the distortion corrected EPI pair (DW) are compared in (B).